Materials Views
www.MaterialsViews.com

ADVANCED FUNCTIONAL MATERIALS
www.afm-journal.de

FEATURE ARTICLE

Electron Transport at the Nanometer-Scale Spatially Revealed by Four-Probe Scanning Tunneling Microscopy

An-Ping Li, Kendal W. Clark, X.-G. Zhang, and Arthur P. Baddorf*

Electron transport at the nanometer-scale is the key to novel applications of nanomaterials in electronic and energy technologies. Due to the restricted dimensionality, one of the distinctive characteristics of nano-systems is their transport properties critically depend on structural details. Therefore, an important requirement for transport research of a specific nanomaterial system is to examine structures and properties in a coherent manner. In this regard, four-probe scanning tunneling microscopy (STM), which combines four independently controllable STMs with a scanning electron microscope (SEM) in the same cryogenic environment, is uniquely useful for probing electron transport on multiple length-scales and revealing how transport is coupled to the electronic and structural properties down to the atomic scale for individual nanomaterials. By utilizing this unique tool, extensive research has been undertaken to explore aspects of nanotransport, which include (a) intertwined electronic and structural phase transitions in surface supported two-dimensional structures, (b) effects of atomic defects and interwire coupling on the electronic and transport properties of ultra thin quantum wire systems, (c) grain boundary resistances in copper nanowires with one-to-one correspondence to the grain boundary structure, (d) defect scattering effects in two-dimensional electron gas systems, and (e) evaluation of transport behaviors of individual semiconductor nano-junctions and nanodevices. In this paper, transport measurement techniques are first introduced with a four-probe STM and then the recent progress on its applications is reviewed with a focus on the spatially resolved electron transport at the nanometer-scale. The goal is to stimulate further advancement and utilization of techniques capable of characterizing materials properties at the nanometer-scale to facilitate the exploration of the great promise of nanoscience and nanotechnology.

1. Introduction

The progress of condensed matter physics and material science in the past two decades has followed in large part the scaling to ever smaller length scales of the samples under study, enabled by advances in the tools used for fabrication and manipulation of these samples. Development of nanotechnology has enabled creation of a variety of nanomaterials with the characteristic size of only a few nanometers.[1] Fundamental study of these materials and structures can only be possible through continued advancement and utilization of techniques capable of characterizing materials properties at the nanometer-scale.[2,3] At the nanometer-scale, different laws of physics come into play (quantum physics), the broken symmetry effect at surfaces starts to dominate transport behavior, and new modes of physical behavior open up. For electrical transport, in particular, when a conductor of size L is smaller than the electron phase coherence length ξ, the classical Drude conduction mechanism no longer holds, and the system enters a mesoscopic regime of quantum transport, where universal conductance fluctuations become important.[4] When the system size is even smaller and L becomes smaller than the elastic mean free path l, the system enters the ballistic regime where electrons traverse the conductor ballistically without, on average, suffering scattering. In this regime, current is limited by scattering at the boundaries (i.e., contacts) of the conductor, and the conductance is described by the Landauer theory. In addition to the size effect, electron-electron interactions, hot-electrons, and microscopic doping gain importance in a low-dimensional system, and the reduced dimensionality can lead to qualitatively different transport than bulk materials.[5]

As a salient example, nanowires have been a focus of many studies, where quantum confinement of the electron states may come into play in the transverse directions, so that only a small number of discrete electron states are available for conduction. For this reason nanowires are also often called quantum wires. Because of the geometric confinement, the presence of defects can have a much more pronounced effect on transport at the nanometer-scale than in three-dimensional (3D) macroscopic solids. In a macroscopic solid, where there are a large number of conduction channels, the presence of a defect will usually merely scatter electrons from one channel into other channels. This will give a contribution to the resistivity but in general, a single defect cannot shut down a conduction channel, so its effect on the total resistivity is small. The combined effect of a

Dr. A.-P. Li, Dr. K. W. Clark, Dr. X.-G. Zhang,
Dr. A. P. Baddorf
Center for Nanophase Materials Sciences
Oak Ridge National Laboratory
Oak Ridge, TA 37831, USA
E-mail: apli@ornl.gov

DOI: 10.1002/adfm.201203423

large number of defects determines the bulk transport property. In nanowires, however, there are very few conduction channels to scatter into. In addition, the coupling between the channels depends strongly on the symmetry of the nanowire and those of the electron wave function. Thus, a single defect can dramatically change the conductance of the entire wire. It may even shut down a conduction channel completely. It is therefore important to study electron transport in nanometer-scale structures in a spatially resolved manner, especially near defects and boundaries.

Measuring electron transport behavior in these nanomaterials presents a significant challenge. Conventional transport electrodes and probes are very invasive; namely, they change what is trying to be measured. For a large conductor, the probes only represent a minor perturbation. But for a small conductor, especially at the nanometer-scale, the probes can very well be the dominant source of scattering. One especially important tool for probing local electronic and transport properties is STM.[3] Whereas the STM mode provides the topography and allows possible structural or electronic features of the materials to be revealed, the scanning tunneling spectroscopy (STS) mode allows the observation of electronic spectral properties with atomic resolution. STM has not only been used to image surface structure on the atomic scale but also led to the development of various new microscopes such as the atomic force microscope (AFM).[2] These are collectively known as scanning probe microscopes (SPMs),[6] which provide unparalleled access to the nanometer-scale world through structural imaging, functionality probing, and nanostructure manipulation. Ever since its invention, SPM has evolved into a powerful measurement technique and has enabled us to observe electron transport on the nanometer-scale, revealing a rich spectrum of information unavailable to macroscopic transport measurements. The uniqueness of an electron transport study with a SPM lies in the correlation of transport with a broad range of other material properties like, topographic, electronic, magnetic, optical, mechanical, and electrochemical, at the level from atomic to mesoscopic length scales.

2. Transport Measurement Method with Four-Probe STM

Electrical conductivity can be measured with SPM through probing the specific conductance of the material directly below the tip by measuring the local current induced by the potential applied to the sample.[7] This set of techniques employs only one movable probe and is invariably based on measuring tip-surface current in contact or tunneling mode. If the tip-surface contact resistance is small (good contact), the current will be limited by the spreading resistance of the sample from which the specific resistance can be calculated, assuming that the contact area is known. In practice good tip-surface contact requires high indentation forces and extremely clean surfaces, which makes the technique highly invasive. On semiconductor and poorly conducting surfaces, space charge layers and Schottky regions below the tip will also affect the measurements.

Alternatively, conductivity measurements can be made based on potential-sensitive SPM techniques on laterally biased surfaces, such as scanning surface potential microscopy specifically Kelvin probe force microscopy (KPFM)[8] and scanning tunneling potentiometry (STP).[9] This setup is very similar to the usual 4 point resistivity measurements, but instead of two fixed voltage electrodes, the SPM tips can act as a moving voltage electrode.[10]

An-Ping Li is a staff scientist in Center for Nanophase Materials Sciences, Oak Ridge National Laboratory with an adjunct professor appointment in The University of Tennessee. He received his PhD degree in physics from Peking University in 1997 and joined ORNL in 2002. He currently manages a cryogenic mutiple-probe scanning tunneling microscope facility. His research mainly concerns controlled synthesis and functional imaging of nanostructured materials for energy applications.

In the last decade, several groups have developed four-probe STM that can perform four-point electrical measurements with probe spacing down to the microscopic scale.[11–14] A recent review on the development of multiple-probe STM has been provided by Nanayama et al.[15] For these systems, a uniform temperature control for the sample and all STM probes greatly improves the system capability. If transport experiments involve electrons injected from hot probes into samples at much lower temperature, such a temperature gradient between the probe and the sample will severely impact the stability and thus the reliability of the experiments. Moreover, injected hot electrons will take a long time to reach thermal equilibrium with the sample (lattice temperature) usually through an electron-phonon coupling that is very weak at low temperatures, imposing an additional level of complexity to the interpretation of the experiments. Although the temperature management in these multiple-probe STM systems is a serious challenge, several systems have demonstrated a cryogenic multi-probe STM capability,[11,13] where multiple functional modules are integrated in a single system with a uniform temperature control.

Figure 1 shows the picture of a cryogenic four-probe STM system at Oak Ridge National Laboratory. The instrument has been described in detail elsewhere.[13] Briefly, four independently controllable STM probes are integrated with an SEM in an ultra-high vacuum (UHV) chamber. The capabilities include material synthesis, high resolution microscopy, chemical analysis, cryogenic temperature control both for sample and probes, atomic resolution imaging and spectroscopy, four independently controllable STM probes, and local electrical transport probing. This four-probe STM (Unisoku) builds on the experience of one previous cryogenic four-probe STM in which both sample and probes are kept at the same low temperature.[16] Each of the four probes works independently as a cryogenic STM, and together, they provide the capability of

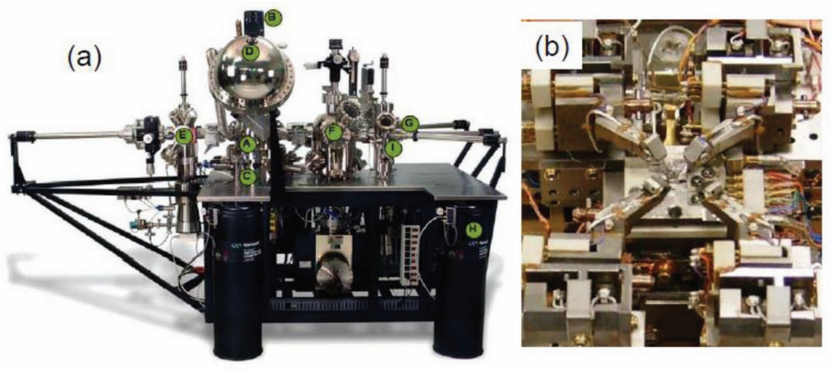

Figure 1. The RHK/Unisoku four-probe cryogenic STM system. a) An overview picture of the four-probe STM system, where A: four-probe STM, B: SEM, C: Cryostat, D: Electron energy analyzer, E: Probe load lock, F: MBE chamber, G: Sample load lock, H: Air leg, I: Sample cleaving chamber. b) Picture of STM probe and sample stage.

four-point electrical transport measurement for nanostructured materials. The SEM is compatible with UHV and has a spatial resolution of about 10 nm. Each STM tip can achieve atomic resolution imaging and spectroscopy, with a coarse motion range of 4 mm × 5 mm × 3 mm (*x, y, z*) and scanning range of 1.5 μm × 1.5 μm × 1.5 μm at room temperature. And the sample stage has a motion range, namely the workspace for manipulation, of 10 and 5 mm in *x* and *y*, respectively. The spatial positioning resolution of the piezoelectric actuator-driven probes and sample stage is down to 0.1 nm. The control system (RHK Quadraprobe) utilizes a computer based control and data analysis system to provide synchronized control of 3D probe coarse positioning of all four probes, 3D fine positioning of each probe, a 2D coarse positioning of the sample stage. With this setup, operations such as pushing, bending, slicing, burning, and cutting of nano-objects can be performed by controlling the four probes in a synchronized fashion.[17] STM and SEM imaging and electrical transport can be carried out on a variety of nanostructured samples.

2.1. Four-Point Contact Measurement Method with Four-Probe STM

In the transport measurement with a four-probe STM in a linear arrangement on a nanowire, the outer pair of probes touch a sample surface and a voltage is applied between them, resulting in a current I flowing through the sample, as shown in **Figure 2**. The inner pair of probes record a voltage drop V along the surface due to the resistance of the sample. Thus one can obtain a four-point-probe resistance $R = V/I$. Owing to this configuration, one can ideally measure the resistance of a sample without any influence of contact resistance at the probe contacts, irrespective of whether the probe contacts are ohmic or Schottky-type.[18] This is because a negligible current flows through the inner pair of contacts, so that no voltage drops at the probe contacts occur. This is a great advantage in the four-point probe method.

The four-point geometry frequently used for macroscopic measurements is a square arrangement as suggested by van der Pauw.[19] For a more general four-probe measurement, where the position of each probe is arbitrary on a sample surface, the measured resistance from the four-probe setup is defined as

$$R = \frac{|\phi(\mathbf{r}_3) - \phi(\mathbf{r}_4)|}{I} \tag{1}$$

where $\mathbf{r}_3$ and $\mathbf{r}_4$ are the positions of the voltage probes. Each current probe is assumed to provide a point source (drain) for the current. If the total current is I, then the electrostatic potential satisfies the Poisson equation

$$\sigma\nabla^2\phi(\mathbf{r}) = -I\left[\delta(\mathbf{r}-\mathbf{r}_1) - \delta(\mathbf{r}-\mathbf{r}_2)\right] \tag{2}$$

where σ is the uniform conductivity, and the positions of the current source (drain) probes are at $\mathbf{r}_1$ and $\mathbf{r}_2$, respectively.

For a 2D system, the solution for the potential is

$$\phi(\mathbf{r}) = \frac{I}{2\pi\sigma_s}\ln\frac{|\mathbf{r}-\mathbf{r}_1|}{|\mathbf{r}-\mathbf{r}_2|} \tag{3}$$

where σ_s is the surface conductivity. Thus the measured resistance is related to the surface conductivity by

$$R_{2D} = \frac{1}{2\pi\sigma_s}\left|\ln\frac{s_{13}s_{24}}{s_{23}s_{14}}\right| \tag{4}$$

where s_{ij} is the separation between probes i and j. For a square configuration with both current probes on one side of the square and voltage probes on the other and equal probe spacing, $R_{2D} = \frac{\ln 2}{2\pi\sigma_s}$. And for a linear configuration with equal probe spacing, $R_{2D} = \frac{\ln 2}{\pi\sigma_s}$.

For a semi-infinite 3D system, the solution for the potential is

$$\phi(\mathbf{r}) = \frac{I}{2\pi\sigma_b}\left(\frac{1}{|\mathbf{r}-\mathbf{r}_1|} - \frac{1}{|\mathbf{r}-\mathbf{r}_2|}\right) \tag{5}$$

whereσ_b is the bulk conductivity.[20] The measured resistance is then related to the bulk conductivity by

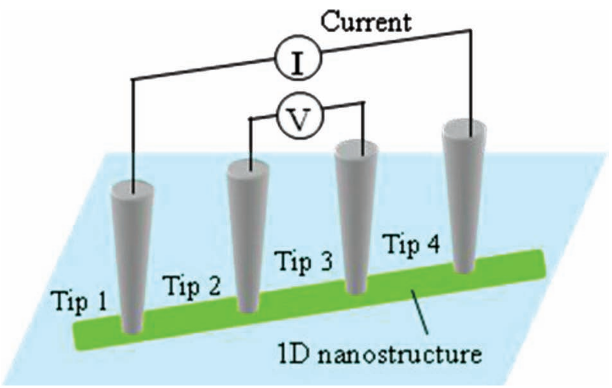

Figure 2. Schematic drawings of the four-point probe method in linear arrangements on a 1D nanostructure.

$$R_{3D} = \frac{1}{2\pi\sigma_b}\left|\frac{1}{s_{13}}+\frac{1}{s_{24}}-\frac{1}{s_{23}}-\frac{1}{s_{14}}\right| \tag{6}$$

One characteristic of uniform conductivity is that the measured resistance is the same when the current and voltage probes are interchanged, i.e., one should measure the same resistance whether using 1, 2 as the current probes or using 3, 4 as the current probes. Thus the difference $R_{1,2} - R_{3,4}$ can be considered as a measure of the nonuniformity of the conductivity. When it is zero, the conductivity is completely uniform.

When the conductivity is not uniform, then the Poisson equation needs to be modified as

$$\nabla \cdot [\sigma(\mathbf{r}) \nabla \phi(\mathbf{r})] = -I[\delta(\mathbf{r}-\mathbf{r}_1) - \delta(\mathbf{r}-\mathbf{r}_2)] \tag{7}$$

This equation is usually solved numerically, for example, using a finite element method.[21]

2.2. Scanning Tunneling Potentiometry Measurement Method with Four-Probe STM

Another method of measuring spatially resolved 2D transport using a four-probe STM is scanning tunneling potentiometry.[9,10] The procedure for recording the STP measurement requires two probes contacting the sample surface with a fixed current flowing between them, as schematically shown in **Figure 3**. A third probe is positioned between the two current probes and scans the sample surface to map the electrochemical potential distribution. The close proximity of the two current probes allows the voltage drop to be large with a small applied current, both protecting the surface and probes against damage and allowing a larger signal to be detected at the center scanning probe. Obviously, the spatial resolution of STP is optimized by imposing the largest possible voltage drop throughout the sample. By taking into account the fact that at room temperature, the intrinsic resolution in voltage (ignoring the instrumental resolution) is mainly limited by the thermal noise in the junction (ca. 1 μV at 300 K), a 1 nm spatial resolution requires applying electric fields of the order of 1 V/mm or more. Therefore, using STM probes with small probe spacing will greatly improve the spatial resolution of STP.

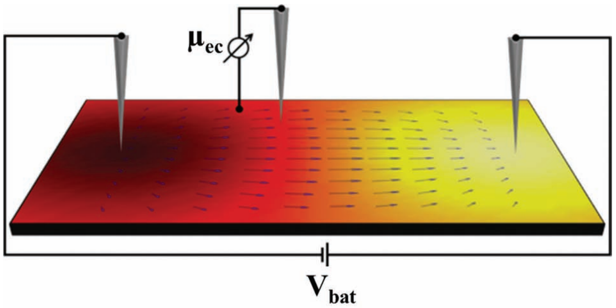

Figure 3. Schematic of the STP experimental setup of a thin conducting layer on a sample surface. Two outer probes are in contact with the conducting layer applying a current through the surface layer. The resulting electrochemical potential distribution $\mu_{ec}(x,y)$ is sketched by the color gradient, the calculated electric field lines are shown with arrow bars as well. STM probe in-between the source probes scans across the surface and simultaneously maps the topography and the potential distribution.

STP uses the tip of an STM as a weakly coupled, noninvasive voltage probe to determine the spatial variation of the local electrochemical potential $\mu_{ec}(x,y)$ on the surface of a current carrying sample. This quantity characterizes the electronic energy level filling in a nonequilibrium situation and its gradient will (assuming a constant density of carriers) describe local electric fields connected with the electric transport.[22] Since the invention of STP by Muralt and Pohl[9] different STP implementations have been presented,[23] and the development of the STP technique was reviewed by Baddorf.[24] Two approaches have been mainly used to separate signals from topography and potentiometry. The first, used in the original experiments by Muralt et al.[9] uses AC current to control the tip-surface separation and DC current to identify the voltage drop across the sample which can be distinguished using a lock-in technique. With this approach the topography and potentiometry signals are measured simultaneously. The second approach, introduced by Feenstra and co-workers,[25] uses an interrupted feedback, first measuring the surface topography, and then retracing that topography with the feedback off to determine the potentiometry.

The experimental procedure of STP measurements adapted for a four-probe STM is described as follows. In the simultaneous AC and DC feedback approach to separating topographic and potential signals in STP, the potential map is directly recorded as the probe scans across the sample. This is achieved by using a separate feedback circuit that adjusts the bias voltage to maintain zero DC tunneling current. This bias value is a direct measure of the potential. The probe is maintained without contacting the sample due to the AC noise current that is always present between the tip and sample. This technique has been referred to as "scanning noise potentiometry".[24] The bias is recorded along with the z value to obtain both a map of the potential distribution as well as the sample topography. The interrupted feedback approach to separating topographic and potential signals in STP has its origins in the "sample and hold" technique of Feenstra and coworkers.[25] The "sample and hold" method was developed to accurately measure *I*–*V* curves in STP. First topology, or tip height for a single point, is determined in the usual way, with the feedback loop to the z piezo active. The feedback loop is then interrupted and the tip (or sample) bias used for topographic scanning switched off. With the tip held at a fixed position, *I*–*V* characteristics are quickly measured before drift becomes significant (on the order of a few seconds). The recorded *I*–*V* curve is post-processed by fitting with a linear equation and the bias voltage at zero tunneling current is extracted from the fit. This zero current bias voltage is the potential value at that point on the sample. This process is repeated at each point on the grid to build up the potential map of the surface.

Based on the 2D potential distribution, the direction and magnitude of the components of the local transport field $E(x,y)$ can be obtained through the relation

$$E(x, y) = -\frac{1}{e}\nabla\mu(x, y) \tag{8}$$

The conductivity can then be deduced by solving the conduction equations. The current conservation condition is

$$\nabla \cdot \mathbf{j} = \frac{\partial}{\partial x}(\sigma_x E_x) + \frac{\partial}{\partial y}(\sigma_y E_y) = 0 \tag{9}$$

Additional equations are obtained by assuming $\nabla \times \mathbf{j} = 0$ which means that there are no circular currents. We write out this condition as,

$$\oint (\sigma_x E_x dx + \sigma_y E_y dy) = 0 \tag{10}$$

On a discrete grid, the problem is equivalent to a network of resistors using appropriate boundary conditions.

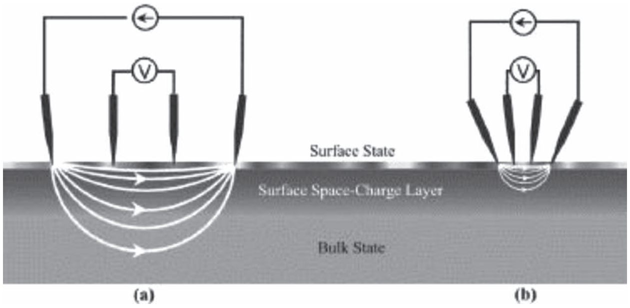

Figure 4. Four-probe STM methods measuring electrical conductance where the current travels through both surface and bulk. The distribution of current flowing through a semiconductor sample is schematically drawn. Reprinted with permission.[16] Copyright 2001, Elsevier Science B. V.

3. Conductance of Metallic Surface States on a Semiconducting Surface

Ever since its development, four-probe STM has been widely used to measure the local electrical conductance of well-defined crystal surfaces in UHV, on which the S. Hasegawa group in Tokyo has played a pioneering role.[16,26,27] The surface states on crystal surfaces are known to have characteristic electric band structures that are sometimes quite different from that in the bulk, which provides a promising playground for studying low-dimensional transport phenomena. As schematically drawn in **Figure 4**, when measuring a semiconductor crystal the current will in principle flow through three channels in the sample:[16] (1) surface states located on the topmost atomic layers, (2) bulk states in the surface space-charge layer beneath the surface (when the bulk bands bend beneath the surface, the carrier concentration can be different from that of the inner bulk), and (3) bulk states in the interior of crystal (which do not depend on the surface structures and states). If one makes the probe spacing as small as the thickness of the space-charge layer or less, as shown in the right panel of Figure 4, the measurement current will mainly pass through the surface region only, and the bulk contribution to the resistance measurement will be largely suppressed. This microscopic four-point probe method thus has a higher surface sensitivity. Furthermore, by placing the four probes at the center of a macroscopic sample surface, the sample can be regarded as infinitely large, so that the measured resistance can be analytically calculated by solving the Poisson equation as described early.

To perform four-point electrical transport measurements, SEM and STM observations can be used to guide the positioning of probes on a sample surface with nanometer spatial precision. The wide dynamic range of currents necessary for both tunneling operation and direct current measurements is provided by variable-gain preamplifiers. The STM feedback current will increase dramatically once a probe is in physical contact with the sample. During the initial probe navigation using the SEM, the “electron shadow” of the probes in the SEM images is used to estimate the distance between the probe and the sample.[13] Final navigation of the probes is performed using the STM approach function. The STM feedback loops are then de-activated when the tunneling junction is established and the probes can be manually approached further toward the sample surface with precision on the nanometer scale by controlling the piezo scanner z-offset. To avoid any influence from high energy electrons, the SEM beam is blocked during measurements.

We first demonstrate the transport measurements on surface domains formed by Au-induced surface reconstructions on Si(111). When the surface is covered by a small amount of Au (less than 0.2 ML), chainlike Si(111)5 × 2-Au surface structures start to form on a Si(111)7 × 7 reconstructed surface.[28] At an optimum coverage with ~0.44 ML of Au, the Si(111) 7 × 7 surface can be converted to a single domain of Si(111)5 × 2-Au.[28] At the coverage of Au between 0.2 and 0.4 ML, a mixed surface layer with domains of both Si(111) 7 × 7 and Si(111)5 × 2-Au can be seen in STM images (**Figure 5**a). By locating all four probes into individual domains, the transport behaviors of these two systems can be examined with the four-probe STM. Figure 5b shows *I*–*V* curves of two different surface domains measured at 85 K. The *I*–*V* characteristics clearly display the

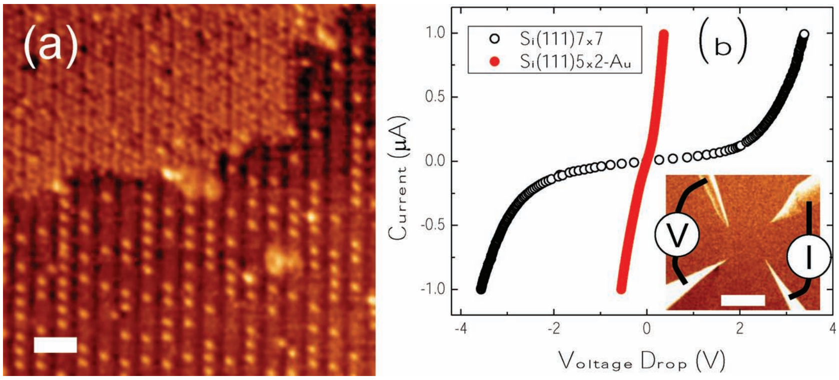

Figure 5. a) Atomically resolved STM images obtained on Si(111)7 × 7 (upper part) and Si(111)5 × 2-Au (lower part), scale bars correspond to 4 nm. b) *I*–*V* curves of Si(111)7 × 7 (open circles) and Si(111)5 × 2-Au (solid circles) obtained by four-point measurement at 85 K. Inset shows the arrangement of four probes and electrical connection. Adapted with permission.[13] Copyright 2007, American Institute of Physics.

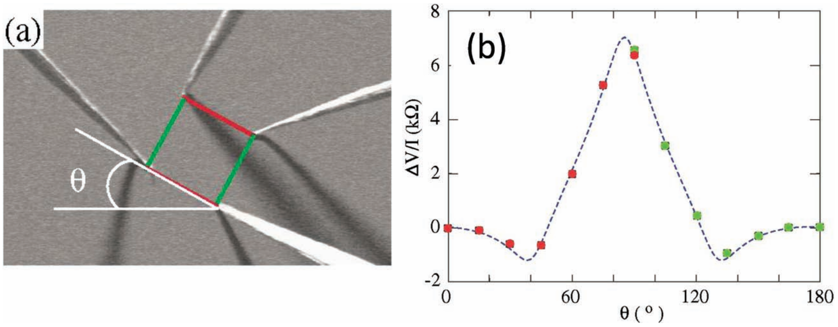

Figure 7. a) SEM image of rotational square micro-4-point-probe measurements with 60 μm probe spacing, with an orientation angle θ. b) Angle dependence of the measured resistance of the single-domain 4 × 1-In surface. Adapted with permission.[27] Copyright 2003, American Physical Society.

difference of surface conductance between Si(111)7 × 7 reconstructed and Si(111)5 × 2-Au surface structures. While the Si(111)7 × 7 surface displays a semiconducting behavior, the Si(111)5 × 2-Au surface shows a much higher conductance with non-linear behavior at low bias voltage. Previous studies suggested that the Si(111)5 × 2-Au surface is either metallic or semiconducting along the atomic chains depending on the concentration of Si adatoms.[29] The Si(111)7 × 7 surface is believed to be metallic based on electron counting arguments and photoemission investigations.[30] However, surface sensitive conductance measurements and NMR studies have indicated that the surface is clearly not in the metallic regime, but close to a Mott–Hubbard-type metal–insulator transition.[20,31] Our conductance measurement here also indicates a much reduced conductivity at low temperature.

The capability of measuring local conductance can greatly facilitate the study of electronic phase transitions in low-dimensional systems. Since electrical transport in low-dimensional systems is affected by atomic disorder and defects much more than in three-dimensional bulk materials, it has been thought that it is difficult for such low-dimensional systems to exhibit metallic transport at low temperatures due to defect-induced Anderson localization. However, in recent years, atomic-scale low-dimensional systems showing metallic transport even at low temperatures have been found, such as quasi-1D metallic states in a wide range of quantum wire systems from single-wall carbon nanotubes[32,33] and quasi-1D surface reconstructions induced by Au or In on both planar and high-index Si surfaces.[34,35] Currently the most prominent metallic low-D system is graphene, a monatomic layer of carbon.[36]

Based on four-probe transport measurements, Kanagawa et al. have revealed an anisotropic electric conductance in a surface reconstruction layer formed by In on the Si(111) surface.[27] The 4 × 1-In surface was prepared by In deposition onto a well-cleaned Si(111)7 × 7 surface at 400 °C. A vicinal Si wafer with 1.8° miscut from the (111) axis was used to grow a single-domain 4 × 1 phase. **Figure 6** shows *I–V* curves measured by the square micro-4-point-probe method with 60 μm probe spacing. The results indicate that an exchange of current flow from parallel to perpendicular with respect to the metallic In chains results in ~60 times difference in the measured resistance. This clearly demonstrates a detection of the anisotropy in conductance, and also means a direct detection of surface-state conductance (because the substrate conductance is isotropic). The anisotropic conductance was further confirmed by rotating the four-point-contact square configuration around its center. The results are shown in **Figure 7**. The rotation angle is defined by two current probes with respect to the In-chain direction. The Poisson equation gives an analytical form for resistance as a function of θ measured by this "rotational square micro-four-point-probe method":

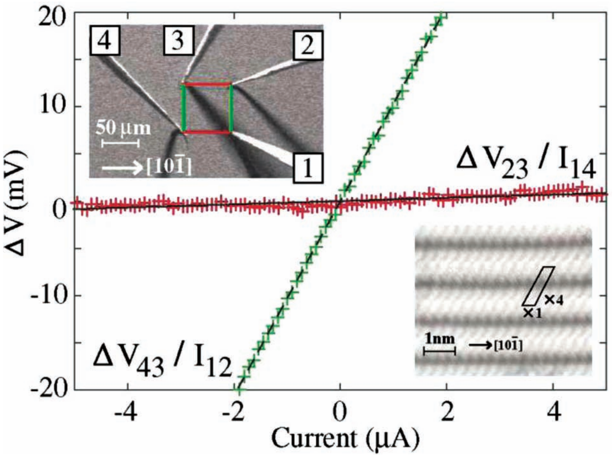

Figure 6. *I–V* curves of a single-domain Si(111)4 × 1-In surface. The upper left inset is a SEM image of the probes. The lower right inset is a STM image of the 4 × 1-In surface. Reproduced with permission.[27] Copyright 2003, American Physical Society.

$$\frac{\Delta V}{I} = \frac{1}{2\pi\sqrt{\sigma_x\sigma_y}} \times \ln\sqrt{\frac{\left(\sigma_x/\sigma_y+1\right)^2 - 4\cos^2\vartheta\,\sin^2\theta\left(\sigma_x/\sigma_y-1\right)^2}{\left(\sin^2\theta+\sigma_x/\sigma_y\cos^2\vartheta\right)^2}} \quad (11)$$

By fitting this with the experimental data[27] in Figure 7, σ_x and σ_y were determined to be 7.2×10^{-4} and 1.2×10^{-5} S/sq., respectively, its anisotropy being ~60.

More recently, Yamazaki et al. have studied the temperature dependence of the surface conductance on a variety of surface reconstructions formed by In on the Si(111) surface.[37] They reported that the $\sqrt{7} \times \sqrt{3}$ surface exhibits a monotonically decreasing resistivity with cooling (metallic temperature dependence) from RT to 10 K, while the $\sqrt{3} \times \sqrt{3}$ and the $\sqrt{31} \times \sqrt{31}$ surfaces are insulating and the 4 × 1 surface exhibits a metal-insulator transition driven by Peierls instability at low temperatures. This is the first report, with the exception of graphene, showing a monatomic layer with a higher conductivity than the minimum metallic conductivity as well as metallic temperature dependence of resistivity.

4. Electronic Transport in Quantum Wires

Quantum wires are extremely narrow 1D materials where electron motion is allowed only along the wire direction, and is confined in the other two directions. Quantum wires, as the smallest electronic conductor, are expected to be a fundamental component in all quantum electronic architectures. The electronic conductance in quantum wires, however, is often dictated by structural instabilities and electron localization at the atomic scale. Experimentally, the local electronic structures of quantum wires and wire arrays are commonly probed by using STM and angular resolved photoemission spectroscopy. A finite density of states (DOS) near the Fermi level, suggestive of metallic characteristics, has been revealed in a wide range of 1D systems from single-wall carbon nanotubes[32] to quasi-1D surface reconstructions induced by Au or In on Si surfaces.[34] However, the local DOS exhibits a spontaneous metal-insulator transition (MIT) at low temperature due to a symmetry-lowering lattice deformation or charge density re-organization in most 1D systems.[34,35,38] A metallic band structure has been revealed in $GdSi_2$ nanowires,[39] while a fluctuating charge order has also been reported in YSi_2 nanowires at low temperatures.[40] Four-probe STM provides the first real opportunity to explore the direct correlation between electronic transport and local electronic and structural properties down to the atomic scale, despite several early attempts with other techniques at macro- to mesoscopic length scale.[41]

By using a four-probe STM, Qin et al. have recently examined the intrinsic transport-structure relations down to the atomic scale by growing quantum wire systems wire-by-wire and performing both STM and nano-transport measurements on the same system.[42] The quantum wire system is $GdSi_2$ nanowires self-assembled on the Si(100) surface. Individual nanowires have a width of 16.7 Å, a height of 4 Å, and lengths of micrometers, and embody one of the closest realizations of 1D conductors, as shown in **Figure 8**a. Amazingly, these nanowires can be grown either isolated or in bundles with a number of constituent wires separated by an atomic interwire spacing (Figure 8b). Single nanowires and nanowire bundles display dramatically different transport characteristics. At room temperature, both the single wires and wire bundles exhibit linear I–V, indicative of a metallic conductance and the Ohmic nature of the Au/$GdSi_2$ contacts. At lower temperatures, the linear I–V behavior and the metallic conductance only persist for nanowire bundles consisting of three or more nanowires, as Figure 8c shows for a three-wire bundle. The I–V curves of single nanowires or wire bundles consisting of only two nanowires become non-linear at low temperatures. This suggests a semiconducting (or insulating) nature of the nanowire; namely a metal-insulator transition occurs in the isolated nanowires and the two-wire bundles at low temperature. Moreover, as shown in Figure 8d for a two-wire bundle, the I–V curves are no longer symmetric, suggesting a different coupling condition of the two electrodes. The numerical dI/dV curves display

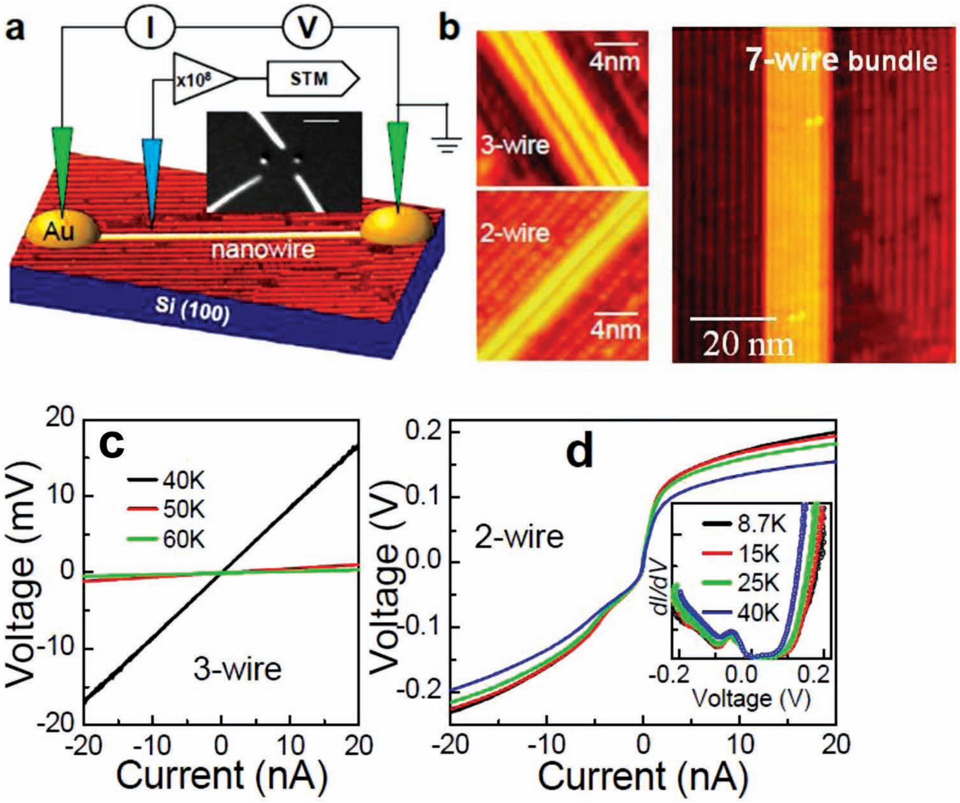

Figure 8. a) A cryogenic four-probe STM is used to probe both the electrical transport and the electronic structures of individual $GdSi_2$ nanowires. b) STM images of self-assembled nanowires with different width. c) Transport I–V curves for a three-wire bundle. d) Transport I–V curves for a two-wire bundle. Insets: numerical transport dI/dV of the two-wire bundle. Adapted with permission.[42] Copyright 2012, American Chemical Society.

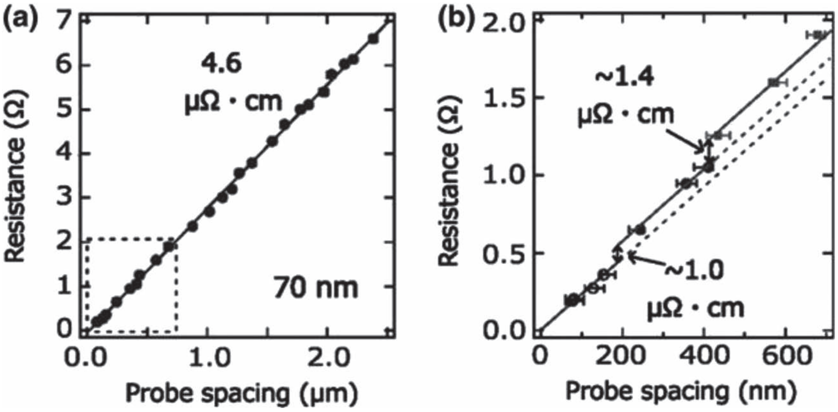

Figure 9. a) The measured resistances of the 70 nm wide Cu wire are shown as a function of probe spacing. b) The enlargement of the graph showing under 600 nm of probe spacing. Reprinted with permission.[46] Copyright 2009, American Institute of Physics.

a clear conductance gap of ~95 mV and a resonance-like peak at about −55 mV (inset of Figure 8d).

These measurements take advantage of our developments in fabricating nanocontacts using a field-induced atom emission process to bridge the atomic wires and the mesoscopic transport electrodes.[43] As the width of the $GdSi_2$ nanowires is much smaller than the STM tip radius, extreme caution is needed to establish reliable contacts for transport measurements. In this application, a gold nano-island (50–200 nm in diameter) was deposited in situ as a local contact at each end of the nanowires via a field-induced atomic emission process.[44] A gold-coated tungsten tip was first located on top of the nanowire in STM scanning mode. The tip then slowly approached the nanowire surface with a 15 V bias applied between the sample and the tip (tip negative). As soon as the tunneling current jumps to ~100 nA, which usually happens at a threshold field of ~3.5 V/Å, Au is being deposited from the tip onto the surface creating Au nano-islands. These contacts serve as electric terminals for in situ transport measurements of the $GdSi_2$ nanowires, as illustrated in Figure 8a. Next, the deposited Au nano-islands were contacted by two new STM tips with Au-coatings directed by the integrated SEM of the four-probe STM system.

This is the first correlated study of electronic properties utilizing both scanning tunneling microscopy and nanotransport measurements on the same nanowire as the nanowires are assembled wire-by-wire, which allowed for a direct examination of the correlation between structure, electronic properties, and electronic transport in the quantum wire system. A metal-insulator transition is revealed in isolated nanowires, while a robust metallic state is obtained in wire bundles at low temperature. Observations are interpreted as atomic defects leading to electron localization in isolated nanowires, and interwire coupling which stabilizes the structure and promotes metallic states in wire bundles. This is a powerful demonstration of the four-probe STM application in probing nanomaterial properties, which provides a rare glimpse of the intrinsic structure-transport relations and the influence of local environments at an unprecedented atomic scale.

5. Structural Dependence of Grain Boundary Resistance in Cu Interconnect Wires

The nanometer-scale transport capability of the four-probe STM allows probing not only of microscopic domains but individual domain boundaries as well. A good example of this application is the measurement of grain boundaries in Cu interconnect nanowires. Copper is the current interconnect metal of choice in commercial integrated circuits. As interconnect dimensions decrease, the resistivity of copper increases dramatically because of electron scattering from surfaces, impurities, and grain boundaries (GBs), and threatens to stymie continued device scaling.[45] Understanding the relative importance of these scattering mechanisms has largely relied on semiempirical modeling due to the lack of direct measurements of individual scattering sources. Using the four-probe STM, the first attempt was made to measure individual GB resistances in copper nanowires with one-to-one correspondence to the GB structure.[45,46]

Kitaoka et al.[46] have studied the Cu wires having the width between 70 nm and 1 µm prepared using a Cu/Low-k damascene processes. The Cu nanowires are not single-crystalline; they consist of small grains. By the electron back-scatter diffraction (EBSD) method, such grains are visualized along the Cu damascene lines.[46] Resistance values are measured with a four-probe STM as a function of the probe spacing between the contact points of the voltage probes on the Cu wires (**Figure 9**). For all wires, the probe spacing dependence of resistance basically showed a linear one-dimensional feature, meaning a diffusive transport. It was expected that there would be some change in the resistance when the probe spacing becomes so short that electrons do not undergo grain boundary scattering. To test this expectation the probe spacing was reduced to a scale which is comparable with the grain size where this effect is indeed observed. Figure 9b shows the enlarged view of the data shown in Figure 9a for the probe spacing smaller than 600 nm. There is a slight jump in resistance when the probe spacing is shorter than 200 nm. This must come from the grain boundary scattering where additional resistance occurs at the grain boundary due to the reflection of the electron wave.

Using a similar approach, Kim et al. have furthermore measured the resistance of different types of GBs with a four-probe STM.[45] The Cu wires were fabricated using a focused ion beam from an electroplated uniform film on a silicon substrate. Grain boundaries have been classified as either coincidence lattice site boundaries or "random boundaries."[47] Coincidence boundaries are formed between grains that hold a number of lattice sites in common.[47] The simplest coincidence boundary is the twin boundary, where the reciprocal density of common lattice points in the two grains (Σ) is 3. A GB with misorientation beyond Brandon's criterion[47] is defined as a random boundary. The crystallographic orientations of grains on the copper sample were analyzed by EBSD technique. The inverse pole figure EBSD

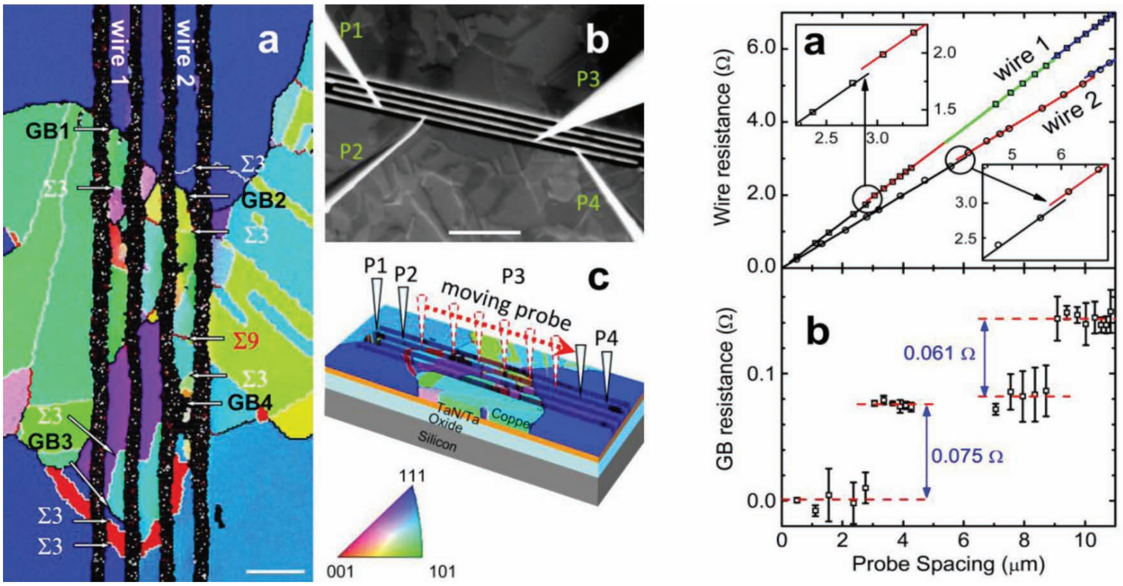

Figure 10. Left Figure: Microstructures of copper nanowires. a) The inverse pole figure of EBSD map showing the crystallographic orientations of grains in the copper sample. (b), SEM image showing four-probe STM contacted onto the same copper nanowire. c) A schematic illustrating the sample structure and the resistance measurement procedure. Right Figure: Resistance jumps near random grain boundaries. a) Measured nanowire resistances as a function of probe spacing at room temperature. Solid line: linear least-square fitting. b) Resistance jumps near random grain boundary on a nanowire obtained by subtracting the bulk resistance contributions from grains. Adapted with permission.[45] Copyright 2010, American Chemical Society.

image is shown in **Figure 10**a. The colors give the crystallographic direction of the local surface normal. The Cu lines contain a high fraction of coincidence GBs (white for $\Sigma3$ and red for $\Sigma9$) with a few high-angle random GBs, typical for electroplated Cu films.[48] The misorientations of some GBs (marked in Figure 10a) are given below in the Bunge axis/angle notation:

Random GB: GB1 – <753> 45.89°; GB2 – <321> 48.669°; GB3 – <321> 50.72°; GB4 – <952> 48.681° and <654> 46.496°.

Coincidence GB: $\Sigma3$ – <111> 60°; $\Sigma9$ – <110> 38.9°.

The specific resistivities of particular GBs are measured using four-probe STM to establish a direct link between GB structure and the resistance.[13,45] The results of this study uncover the critical role of random GB scattering on the increased resistivity of copper interconnects. By directly measuring both intra- and inter-grain resistance with a four-probe STM, surprisingly large resistance jumps across high-angle random GBs are observed as shown in Figure 10, while the resistance of coincidence boundaries are negligibly small and beyond the measurement resolution.

The measured grain resistivities are (1.710 – 1.796) × 10^{-6} $\Omega\cdot$cm, in comparison to 1.723 × 10^{-6} $\Omega\cdot$cm for the pure bulk copper.[49] Random boundaries all have similar specific resistivity (γ_{GB}) values of (19.0 – 25.9) × 10^{-12} $\Omega\cdot$cm^2, though they have different misorientation axis/angle pairs. In addition, Kitaoka, et al., have detected resistance jumps in the range of 0.12 – 0.17 Ω along copper damascene nanowires,[46] fabricated using a different method. Despite the much higher resistance jumps, from the dimension of their wires,[46] a corresponding γ_{GB} value of (20 – 29)×10^{-12} $\Omega\cdot$cm^2 can be calculated, which is surprisingly close to the measurement by Kim et al.[45]

The resistivities of coincidence GBs have been theoretically calculated by using first-principles methods combined with the Boltzmann transport equation by Kim et al.[45] and by Srivastava et al.[50] The result for twin boundary ($\Sigma3$) is 2.08 × 10^{-13} $\Omega\cdot$cm^2, and about two to three times larger for other GBs. These results show that the γ_{GB} of these coincidence boundaries are one or two orders of magnitude smaller than the measured specific resistivity for random boundaries, and thus are beyond the measurement sensitivity of our four-probe STM technique. High-angle random GBs cannot be modeled by first-principles methods but can be modeled using a simple model of free electrons with random point scatterers.[51] It was suggested that due to the scaling of electron mean free path with the size of the lattice relaxation region at the random GB, a universal specific resistivity is obtained for random GBs which only depends on the Fermi wavelength of Cu,

$$\gamma_{GB} = \frac{h}{2e^2}\frac{3\lambda_F^2}{2\pi} \tag{12}$$

For λ_F = 0.46 nm, one finds γ_{GB} = 13 × 10^{-12} $\Omega\cdot$cm^2, which is close to the experimentally measured values for random GBs. These experimental measurements and theoretical calculations indicate that the high specific resistivity of random GBs is an intrinsic effect of GB scattering.[52] The results thus provide direct evidence on the importance of the GB scattering process, particularly at random GBs, and also suggest a path to suppressing the GB scattering effect in polycrystalline nanowires through the conversion of random GBs into coincidence GBs.

Moreover, Evans' group has examined the resistivity of a variety of metallic nanowires such as Au, Zn, and Ni nanowires using a four-probe STM.[14,53,54] They have found that most of these nanowires displayed resistivities from 10 to as high as 100 times higher than the bulk, however, a near-bulk resistivity was observed on Au nanowires when the nanowires are highly

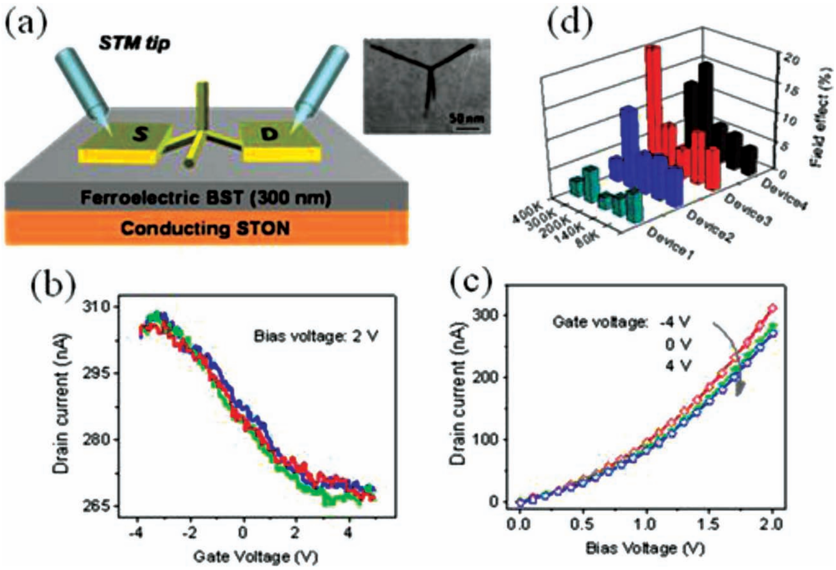

Figure 11. a) A cryogenic four-probe STM is used to probe the electrical transport through individual CdS nanotetrapods with a ferroelectric $Ba_{0.7}Sr_{0.3}TiO_3$ (BST) film as gate dielectric. b) The transfer characteristics of single CdS nanotetrapod device. c) The current versus source-drain bias voltage curves of the nanotetrapod under gate voltages of –4 V, 0 V, and 4 V. d) The temperature dependent variations of the field effect measured for four nanotetrapod devices. Adapted with permission.[55] Copyright 2011, American Chemical Society.

crystalline (few or preferably no grain boundaries) and are highly smooth.[53] The elimination of grain boundaries, especially those random grain boundaries, perpendicular to carrier transport is important for future nanocircuits from the perspective of computational performance, device noise, and energy consumption.

6. Transport in Semiconductor Nanowires and Nanojunctions

Semiconductor nanowire-based heterojunctions and interfaces can also be addressed by using the four-probe STM. The continuing miniaturization of electronic device has inspired extensive research efforts to develop the bottom-up fabrication of unique nanoelectronic devices by taking advantage of the nanostructured materials. Among these nanomaterials, semiconductor nanojunctions and the multi-armed semiconductor nanotetrapods are of particular interest due to their unique nanometer-scale architectures that can deliver functionalities of versatile multi-terminal nanodevices for potential logic circuits, sensors, and memory applications. The experimental testing of the conductance of these nanojunctions calls for a nano-version of a four-probe station that can conveniently access individual arms of the nanojunctions. For semiconductor nanotetrapods, another technological challenge lies in their unique 3D geometric shape that prevents the tetrapod structures from lying flat on the planar substrate surfaces and thus seriously hampers capacitance coupling between the gating electric field and the tetrapod conduction channels. Fu et al. have studied the electrical transport properties of CdS nanotetrapods using a cryogenic four-probe STM[55] at different temperatures as shown in **Figure 11**a. They used a ferroelectric layer with high dielectric constant as a gate dielectric to enhance capacitance coupling with the 3D nanojunctions. As a result, a ferroelectric field effect transistor (FeFET) operation was demonstrated by integrating individual CdS nanotetrapods with the high-*κ*, switchable ferroelectric $Ba_{0.7}Sr_{0.3}TiO_3$ (BST) film as gate dielectric.

Figure 11b shows the current (I_D) versus gate voltage (V_G) characteristics of a tetrapod transistor measured at room-temperature.[55] A *p*-type field effect behavior is seen. The percentage of the current change due to electrostatic field modulation is deduced as $(I_o-I)/I_o \times 100\% = 13\%$, which is significant considering the vacuum gap between the ferroelectric BST dielectric and the tetrapod junction. Figure 11(c) shows the source-drain current versus bias voltage curves of the nanotetrapod under several different gate voltages. When the gate voltage changes from negative to positive, the current decreases gradually, consistent with the *p*-type transfer characteristics. The temperature dependent variations of the field effect measured for four nanotetrapod devices are summarized with a 3D bar plot in Figure 11d. Three out of four devices show maximum field effect at 300 K with another peaking at 400 K. This result correlates well with the temperature dependence of the dielectric constant of the BST ferroelectric film, which exhibits a diffuse transition peak at around 300 K. In addition, the reversible remnant polarization of the ferroelectric gate dielectric allowed observation of a well-defined nonvolatile memory effect. The field effect was shown to originate from the channel tuning in the arm/core/arm junctions of the nanotetrapods. At low temperature (8.5 K), the nanotetrapod devices exhibit a ferroelectric-modulated single-electron transistor (SET) behavior.

This experiment is the first demonstration of a room-temperature ferroelectric field effect transistor in a three dimensional semiconductor nanotetrapod. The enhanced capacitance coupling to nanostructured objects arises from the high dielectric constant of the ferroelectric gate layer. Furthermore, as a consequence of the non-volatile memory effect of the ferroelectric gate dielectric, a proof-of-principle FeFET operation was demonstrated in CdS nanotetrapods at an unprecedented single-electron level. The results illustrate how the characteristics of a ferroelectric such as switchable polarization and high dielectric constant can be exploited to control the functionality of individual three-dimensional nano-architectures.

The combination of nanotransport and nanomanipulation capabilities in the four-probe STM[17,56] make possible examination of the transport behaviors of nanowires while applying mechanic force with STM probes. Lin et al. have demonstrated that after bending ZnO nanowires with the four-probe STM, the conductance is reduced by about five orders of magnitude.[56] The imposed bending deformation of the nanowires is found to be elastic and the induced change of conductance is reversible. It was suggested that strain has a strong effect in changing the alignment of the Fermi level and the electron states of defects in ZnO nanowires whose surface contains a large amount of defects. When the ZnO nanowire is bent, the bending induced surface strain significantly shifts the positions of the surface states, changing their relative position with respect to the Fermi level. Especially, if the strain makes the Fermi level move out of the range of surface states, then the conductance of the ZnO nanowire will decrease continuously as strain (bending) increases. When the strain is removed, the conductance will return to its normal state as the surface states restore their original positions overlapping with the Fermi level.

7. Mapping Conductance with Multiple-Probe STM Scanning Tunneling Potentiometry

Beyond four-point contact measurements, scanning tunneling potentiometry with four-probe STM allows analysis of the potential distribution at a surface while a lateral current is applied to a conducting sample. The key feature of this application is the study of the distribution of the electric current in a two-dimensional electron gas (2DEG) restricted to the surface layer. This enables full local access to the electrochemical potential μ_{ec} by STP. The analysis of the data provides (i) the local electric field as the gradient of μ_{ec}, (ii) the current density, and (iii) the local conductivity at each point in the surface. In addition, the STP determines the spatial variation of the electrochemical potential around individual defects. For locally different directions of the flux of electrons this reveals significant variations of the microscopic conductivity.

7.1. Spatial Variations of the Electrochemical Potential on Si(111)- (√3 × √3)-Ag

STP simultaneously measures the topography of the sample and the local electrochemical potential μ_{ec}. Homoth, et al., have performed STP measurements with a four-probe STM for a well-defined two-dimensional electronic system: the silver-induced (√3 × √3) superstructure on the Si(111) surface.[57] The surface superstructure is formed by covering the surface of a (111)-oriented silicon single crystal with one monolayer of silver. The reconstruction yields a partially occupied electronic surface state providing sufficient conductivity directly accessible at the surface. Electrons in this state behave as a 2DEG, and on n-type silicon charge transport through the 2DEG is electrically isolated from the bulk states of the Si by a space charge layer.

The STP measurement results[57] on Si(111)- (√3 × √3)-Ag are shown in **Figure 12**. As seen in the insets in Figure 12b,e, the lateral current was applied by two gold tips of a three probe STM, which were brought into contact with metallic silver islands in close vicinity (50–300 um) to each other. Figure 12a displays the geometric structure of the area, where most of the steps correspond to monoatomic steps. About one-third of the steps correspond to double steps and a few to triple steps. The terraces in between the steps are atomically flat.

Figure 12b,c show that the local electrochemical potential measured simultaneously with the data of Figure 12a, exhibits only a minor monotonic gradient constant on the terraces with abrupt variation at the step edges. Figure 12d shows cross sections of the topography and μ_{ec} data at a particular step. The variation of μ_{ec} is monotonic and occurs within 6 Å (20–80%). The transition is displaced relative to the step by about 12 Å. The observation of constant values of μ_{ec} on the terraces and abrupt variation at the steps proves that the current transport is restricted to a 2D-layer at the surface and is not affected by the silicon substrate. Figure 12c,f illustrate the calculated potential distributions for the data of Figure 12b,e based on the specific conductivities for the step edge and the 2DEG. The excellent agreement between the calculation and the measured $\mu_{ec}(x, y)$ data is evident.[57]

This experiment gives access to the spatial variations of the electrochemical potential within an electric conductor with nanometer resolution. At a step edge the local electrochemical

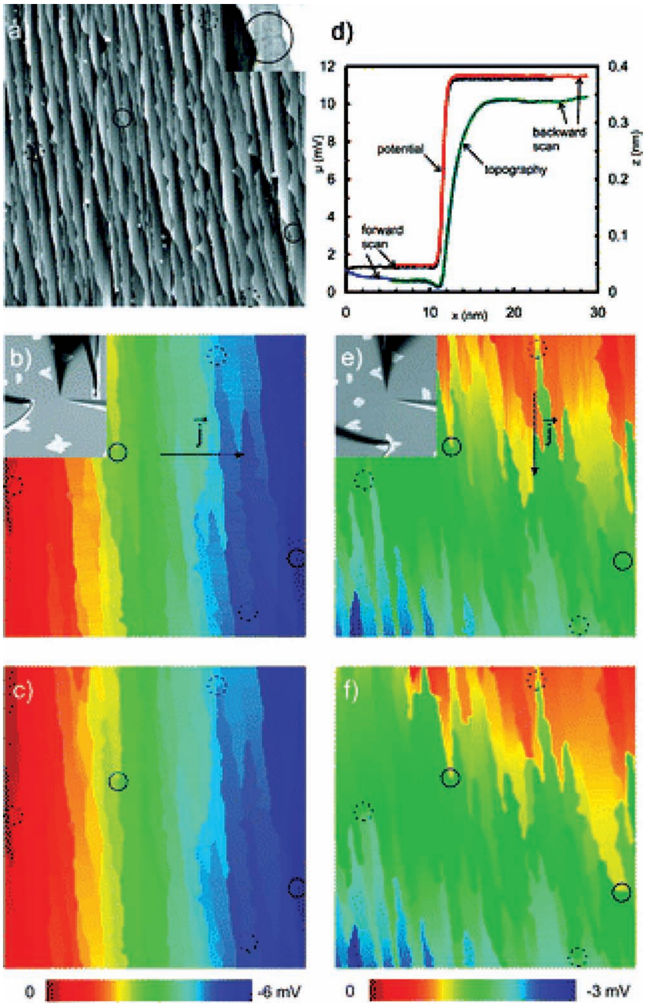

Figure 12. STM and STP of the Si(111)–(√3 × √3)–Ag surface. a) The topographic image. b) The electro-chemical potential simultaneously measured at a current perpendicular to the steps. The result of the corresponding simulation based on a network of "Ohmic" resistors is displayed in (c). d) Line scans across the edge of a monatomic step displaying the tip height in constant conductivity mode. e) The electrochemical potential simultaneously measured at a current parallel to the steps. The result of the corresponding simulation is displayed in (f). Reprinted with permission.[57] Copyright 2009, American Chemical Society.

potential exhibits a rather localized transition. This gives the unique opportunity to evaluate the specific conductivities of the defect free surface and across monatomic steps.

7.2. Domain Boundary Scattering Effects in Graphene

Graphene represents another 2D system that, due to its unique electronic structure, has quickly become one of the most notable "super-materials" with the promise of transforming the electronics and nanotechnology landscape. The symmetry of the graphene honeycomb lattice is a key element determining many of graphene's unique electronic properties. Topological lattice defects break the sublattice symmetry, allowing insight into the fundamental quantum properties of graphene. Yet because of the large length-scale deference between the atoms at defect sites and functionalities that range from atomic to mesoscale, few techniques have the capability of revealing the corresponding relationships between the local structure and the mesoscale properties. The STP technique provides a good bridge of these length scales.

Ji et al. have used STP to measure local electric potential as current flows through a graphene film.[58] By measuring local perturbations caused by substrate steps and changes in graphene thickness, they have demonstrated that such heterogeneity is critical to transport in graphene. Substrate steps alone can increase the resistivity several-fold relative to a perfect terrace, which can be attributed to the intrinsic wavefunction mismatch at junctions between monolayer and bilayer graphene. The performance of graphene devices on SiC surfaces is thus fundamentally limited by the ability to control both the layer thickness and substrate perfection.

Figure 13 shows the results of microscale potential measurements over regions measuring hundreds of nanometres. The topography and graphene thicknesses are shown in Figure 13a. Without applying a voltage between the source probes 1 and 3, the potential map (Figure 13d) is almost featureless. But when a voltage is applied (Figure 13b,e), the maps show dramatic potential jumps at the step edges and a potential gradient on the terraces. These effects change sign when the applied voltage is reversed (Figure 13c,f), showing that the measurement is directly related to transport. Carrier scattering seems to be particularly strong at the heterogeneous junctions between monolayer and bilayer graphene, and weaker but still visible at locations where a uniform graphene bilayer crosses a substrate step (top right corner of each map). Potential profiles across two terraces and a monolayer–bilayer junction are shown for a series of applied voltages in Figure 13i,j. The linear relationships between the terrace gradient and monolayer–bilayer jump and the applied voltage are demonstrated in Figure 13k.

Based on STP results, Ji et al.[58] have found that monolayer graphene crossing single (0.5 nm height) substrate steps show a specific resistivity of 6.9 ± 2.9 $\Omega \cdot \mu$m. The specific resistivity seems to increase linearly with step height, 14.9 ± 3.6 $\Omega \cdot \mu$m for 1.0 nm height steps and 24.7 ± 4.3 $\Omega \cdot \mu$m for 1.5 nm height steps. Monolayer–bilayer junctions have a higher specific resistivity, 20.9 ± 5.7 $\Omega \cdot \mu$m and 28.4 ± 7.0 $\Omega \cdot \mu$m for planar and stepped junctions respectively. Monolayer–bilayer junctions at a double-height step provide the highest specific resistivity seen here, 88 $\Omega \cdot \mu$m. Finally they have found that the current flow can be distorted by the resistive features on the surface. It is interesting to speculate whether spatial control of step configurations could be used to concentrate current into specific regions of a graphene sheet for new device designs.

In a separate work, Clark et al. have applied the STP technique to chemical vapor deposition (CVD) graphene grown on Cu foil and transferred to a SiO_2 substrate.[59] The growth of CVD graphene can be performed in such a way that hexagonal graphene patches are formed on the surface. If the growth is continued the patches will coalesce and form a grain boundary at the interface between the two hexagonal patches. This grain boundary is easily imaged with the SEM located within the four-probe STM (**Figure 14**a) and allows the tips to be positioned to measure the potential across the grain boundary. The STP maps taken across the grain boundary show a step in the potential as the tip scans across the boundary. Figure 14b shows the STM image of the graphene grain boundary and Figure 14c displays the potential step in the simultaneously recorded potential map that corresponds to an increase in resistance at the grain boundary. Further analysis of the grain boundary effect in graphene is discussed separately.[59]

The imaging technique demonstrated here provides the tools to characterize graphene defects and domain/grain boundaries on multiple length scales. These methods will be very useful both for exploring synthesis strategies to optimize defect structures and for the study of the impact of these defects on graphene films.

8. Summary and Outlook

We have reviewed the recent progress in nanocale electronic transport involving four-probe STMs. As a "nano" version of a conventional four-probe station, four-probe STM combines STM local imaging and spectroscopy functions with four-point electrical transport capability in a well-controlled sample environment to produce simultaneous measurements of transport and local structures on nanomaterials. This system provides a platform to study the electron transport properties and the structure relationships over multiple length scales, from individual atoms, molecules, to nanowires and mesoscopic systems. This review focuses on the transport measurements of individual nanostructures, nanojunctions, grain boundaries, and defect lines, which provide a one-to-one correspondence between transport and structures. Applications have extended to a broad range of nanomaterials, such as surface supported quasi-one dimensional and two-dimensional electronic systems, semiconducting and metallic nanowires, carbon nanotubes and graphene, and atomic defects, grain boundaries, and electronic interactions between these nanomaterials. It is noted that electron transport can be studied in several different four-probe configurations. Lateral transport of electrons is studied by using multiple probes to drive a current parallel to the surface and then by measuring either the corresponding potential drops between two probes in contact with the sample area or by measuring the electrochemical potentials using a scanning probe weakly coupled to the sample surface. In this case, the sample is usually placed on an insulating substrate

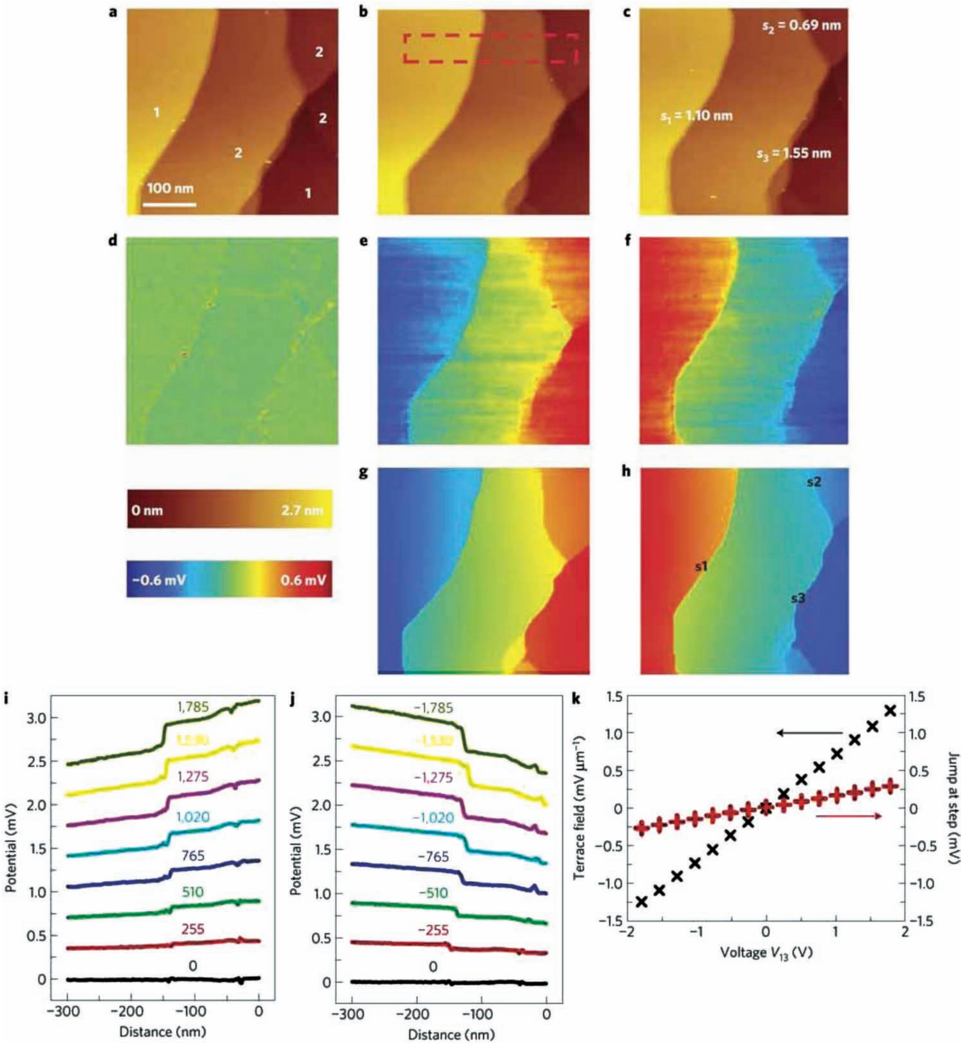

Figure 13. a–c) Topography and d–f) potential maps recorded simultaneously with source $V = 0$ (a,d), $V = 1.53$ V and total current 5.73 mA (b,e) and $V = -1.53$ V (c,f). g,h), Simulated potential maps calculated using the experimental boundary potential conditions. i,j), Line profiles of the potential averaged from the rectangle in (b). Data are offset vertically for clarity. k) The electric field on the terraces (slopes in i and j; monolayer and bilayer terraces being similar) and the potential jump at the monolayer–bilayer junction (jump heights in i and j) as a function of V. Reprinted with permission.[58] Copyright 2011, Macmillan Publishers Limited.

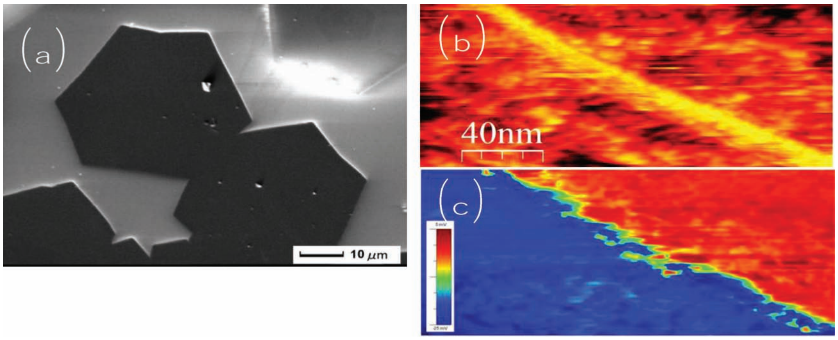

Figure 14. STP mapping of graphene on SiO_2. a) SEM image of coalesced graphene patches. b) STM image of a graphene grain boundary. c) STP potential map across the grain boundary taken simultaneously with STM image (b).

or electrically decoupled from the substrate by a Schottky barrier at the sample-substrate interface. Besides applications in transport studies, four-probe STM can also be used as an operation and manipulation tool for nanostructures[15,17,43,60] and electronic domains,[61] which is beyond the scope of this paper, but once again reinforces the versatility and unique functionality of the four-probe STM.

Since the first demonstration of a double-probe STM in 1998 by Aono et al,[62] great progress has been made in the development and applications of multi-probe STM. New capabilities of four-probe STM, such as in situ SEM and cryogenic operation, have become available for achieving better spatial and energetic resolution. However, the ever-developing demands in materials research now call for further improvement of four-probe STM. Indeed, the promise of nanoscience and nanotechnology can only be realized through continued advancement and utilization of techniques capable of characterizing materials properties at the nanometer-scale. As an outlook of further development in four-probe STM, we believe the progress on these three aspects will be particularly useful for materials research: smaller probe spacing, lower temperature, and optical access.

The achievable minimum probe spacing in electrical transport measurements is a critical factor in determining which transport regime can be experimentally accessible. For studying the quantum transport in a mesoscopic regime, the probe spacing should be smaller than the electron phase coherence length. And for ballistic transport, the probe spacing should be smaller than the elastic mean free path, so that electrons can traverse the conductor without experiencing scattering. In four-probe STM systems, the lateral spacing between probes is adjusted with a combined control of coarse and scan offset motions of the STM. This spacing can be controlled with nanometer precision until the two adjacent probes touch each other. Hence the spacing is only limited by the aspect ratio and apex radius of probes. For a typical tungsten tip etched electrochemically, the tip radius is in the range of 50 nm. And thus, at the present the minimum probe spacing in the multi-probe STM is approximately 50–100 nm. In many cases, this probe spacing is not small enough for observing ballistic transport and quantum interference effects. To make the probe spacing smaller, carbon nanotube probes have been proposed, where a CNT is either grown or glued at the end of a tungsten tip.[63] To reduce the contact resistance and suppress the surface states of CNTs, a metallic layer of W, Pt, or PtIr can be coated onto a CNT probe.[64] With functionalized high aspect ratio probes, it should be possible to achieve a probe spacing of less than 10 nm.

Temperature control down to the critical point, at which multiple electronic, magnetic, or structural phases converge, is another important aspect for expanding the four-probe STM capability. Besides phase transitions, we often rely on measuring the temperature scaling behaviors of conductivity to differentiate various scattering mechanisms that can contribute to the transport process. As a prominent example, the study of superconducting materials requires controlling the sample temperature near and below the superconducting transition point. In this case, a uniform temperature control for all involved sample and probes is necessary not just for establishing a stable probe-sample junction but to maintain a uniform electron and lattice temperature in the whole electron transport network as well. Such a low-temperature four-probe STM will allow for the evaluation of microscopic inhomogeneities of the superconductivity by measuring microscopic variations of superconducting transitions and critical current density.[65] Moreover, temperature control and uniformity are needed to study the proximity effect at the interface of superconductor and normal non-superconductor by measuring the manifested supercurrent flowing through the non-superconductive regions in a microscopic sample region. On this front, several groups have started to develop four-probe STM system with cooling capabilities below 5 K and it becomes desirable to achieve the low temperature capability comparable with a conventional LT-STM.

Optical access to the probe-sample junctions by coupling light in or out of the four-probe chamber will expand the capability to the study of energy conversion and optoelectronic properties in the nanoscopic scale and down to the individual interface level. Since the first demonstration by Gimzewski et al. in 1988,[66] detection of light emission during electron tunneling between a tip-surface gap in the STM has become a useful method for performing local spectroscopy on surfaces. In this photon emission STM, the STM tip is used to inject or accept tunneling electrons to a particular sample location, and light is generated as a result of electron inelastic scattering processes. The emitted light can be collected, analyzed, and finally detected by using a photon detector, providing the optical properties of nanometer-scale regions. A four-probe version of photon emission STM would allow for acquiring an energy-resolved emission spectrum by passing a current across individual sample junctions or interfaces. Alternatively, the scanning electron gun provided by in situ SEM allows for acquiring the cathodoluminescence spectrum by exciting a sample area with the electron beam scanning across a luminescent surface. Moreover, by coupling light into the sample area, the photo-current can be measured by multi-probe STM which provides a powerful tool for probing the photovoltaic effect in nanostructured material. The optical access can be achieved either through free space coupling with lens or mirror near the sample-probe junction or by an optical fiber. In the four-probe STM, an optical fiber can be introduced as a probe that can be independently manipulated by a piezoelectric driver inside the chamber.

In this review, we have attempted to capture some of the exciting science made available by multiple probe STMs. Although the four-probe STM is a relatively new tool, it has demonstrated unique capabilities to explore nanometer-scale functionality through both imaging and spectroscopy of local electron transport at key length scales. As discussed, there remain a number of new directions and prospects that promise to retain interest in four-probe STM for meeting new challenges in materials research.

Acknowledgements

This research was conducted at the Center for Nanophase Materials Sciences, which is sponsored at Oak Ridge National Laboratory by the Scientific User Facilities Division, Office of Basic Energy Sciences, U.S. Department of Energy.

Received: November 21, 2012
Revised: January 13, 2013

---

[1] a) J. V. Barth, G. Costantini, K. Kern, *Nature* **2005**, *437*, 671; b) M. F. Crommie, C. P. Lutz, D. M. Eigler, *Science* **1993**, *262*, 218; c) D. M. Eigler, E. K. Schweizer, *Nature* **1990**, *344*, 524; d) Y. Huang, X. Duan, Y. Cui, L. J. Lauhon, K.-H. Kim, C. M. Lieber, *Science* **2001**, *294*, 1313; e) S. Iijima, *Nature* **1991**, *354*, 56; f) T. A. Jung, R. R. Schlittler, J. K. Gimzewski, H. Tang, C. Joachim, *Science* **1996**, *271*, 181; g) T. Junno, K. Deppert, L. Montelius, L. Samuelson,

Appl. Phys. Lett. **1995**, *66*, 3627; h) A. P. Li, F. Flack, M. G. Lagally, M. F. Chisholm, K. Yoo, Z. Y. Zhang, H. H. Weitering, J. F. Wendelken, *Phys. Rev. B* **2004**, *69*, 5; i) I.-W. Lyo, P. Avouris, *Science* **1991**, *253*, 173; j) K. Yoo, A. P. Li, Z. Y. Zhang, H. H. Weitering, F. Flack, M. G. Lagally, J. F. Wendelken, *Surf. Sci.* **2003**, *546*, L803.

[2] G. Binnig, C. F. Quate, C. Gerber, *Phys. Rev. Lett.* **1986**, *56*, 930.

[3] G. Binnig, H. Rohrer, C. Gerber, E. Weibel, *Phys. Rev. Lett.* **1982**, *49*, 57.

[4] J. Rammer, *Rev. Mod. Phys.* **1991**, *63*, 781.

[5] E. W. Plummer, Ismail, R. Matzdorf, A. V. Melechko, J. P. Pierce, J. D. Zhang, *Surf. Sci.* **2002**, *500*, 1.

[6] S. V. Kalinin, A. Gruverman, *Scanning Probe Microscopy*, Springer, New York **2006**.

[7] S. V. Kalinin, M. R. Suchomel, P. K. Davies, D. A. Bonnell, *J. Am. Ceram. Soc.* **2002**, *85*, 3011.

[8] S. V. Kalinin, D. A. Bonnell, *Phys. Rev. B* **2004**, *70*, 235304.

[9] P. Muralt, D. W. Pohl, *Appl. Phys. Lett.* **1986**, *48*, 514.

[10] A. Bannani, C. A. Bobisch, R. Moller, *Rev. Sci. Instrum.* **2008**, *79*, 083704.

[11] a) V. Cherepanov, E. Zubkov, H. Junker, S. Korte, M. Blab, P. Coenen, B. Voigtlander, *Rev. Sci. Instrum.* **2012**, *83*, 5; b) R. Hobara, N. Nagamura, S. Hasegawa, I. Matsuda, Y. Yamamoto, Y. Miyatake, T. Nagamura, *Rev. Sci. Instrum.* **2007**, *78*, 053705.

[12] a) H. Grube, B. C. Harrison, J. Jia, J. Boland, *J. Rev. Sci. Instrum.* **2001**, *72*, 4388; b) G. Olivier, M. Hubertus, John T. Yates Jr., J. Moon-Chul, L. Jeremy, A. Joachim, *Rev. Sci. Instrum.* **2005**, *76*, 045107; c) T. Shigemi, S. Byron, N. Nobuyuki, *Rev. Sci. Instrum.* **1991**, *62*, 1767; d) T. M. Hansen, K. Stokbro, O. Hansen, T. Hassenkam, I. Shiraki, S. Hasegawa, P. Boggild, *Rev. Sci. Instrum.* **2003**, *74*, 3701.

[13] T.-H. Kim, Z. Wang, J. F. Wendelken, H. H. Weitering, W. Li, A.-P. Li, *Rev. Sci. Instrum.* **2007**, *78*, 123701.

[14] A. S. Walton, C. S. Allen, K. Critchley, M. L. Gorzny, J. E. McKendry, R. M. D. Brydson, B. J. Hickey, S. D. Evans, *Nanotechology* **2007**, *18*, 065204.

[15] T. Nakayama, O. Kubo, Y. Shingaya, S. Higuchi, T. Hasegawa, C.-S. Jiang, T. Okuda, Y. Kuwahara, K. Takami, M. Aono, *Adv. Mater.* **2012**, *24*, 1675.

[16] S. Hasegawa, F. Grey, *Surf. Sci.* **2002**, *500*, 84.

[17] S. Qin, T.-H. Kim, Z. Wang, A.-P. Li, *Rev. Sci. Instrum.* **2012**, *83*, 063704.

[18] F. M. Smits, *Bell Syst. Tech. J.* **1958**, *37*, 711.

[19] L. J. van der Pauw, *Philips Res. Rep.* **1958**, 13.

[20] P. Hofmann, J. W. Wells, *J. Phys.: Conden. Matter* **2009**, *21*, 013003.

[21] J. W. Wells, J. F. Kallehauge, P. Hofmann, *Surf. Sci.* **2008**, *602*, 1742.

[22] C. S. Chu, R. S. Sorbello, *Phys. Rev. B* **1990**, *42*, 4928.

[23] a) T. Druga, M. Wenderoth, J. Homoth, M. A. Schneider, R. G. Ulbrich, *Rev. Sci. Instrum.* **2010**, *81*, 083704; b) R. Moller, A. Esslinger, B. Koslowski, *Appl. Phys. Lett.* **1989**, *55*, 2360; c) J. P. Pelz, R. H. Koch, *Rev. Sci. Instrum.* **1989**, *60*, 301; d) M. Rozler, M. R. Beasley, *Rev. Sci. Instrum.* **2008**, *79*, 073904.

[24] A. P. Baddorf, in *Scanning Probe Microscopy* (Eds: S. V. Kalinin, A. Gruverman), Springer, New York **2007**, p. 11.

[25] a) R. M. Feenstra, W. A. Thompson, A. P. Fein, *Phys. Rev. Lett.* **1986**, *56*, 608; b) A. P. Fein, J. R. Kirtley, R. M. Feenstra, *Rev. Sci. Instrum.* **1987**, *58*, 1806.

[26] a) S. Hasegawa, I. Shiraki, F. Tanabe, R. Hobara, T. Kanagawa, T. Tanikawa, I. Matsuda, C. L. Petersen, T. M. Hansen, P. Boggild, F. Grey, *Surf. Rev. Lett.* **2003**, *10*, 963; b) S. Hasegawa, I. Shiraki, T. Tanikawa, C. L. Petersen, T. M. Hansen, P. Boggild, F. Grey, *J. Phys.: Condens. Matter* **2002**, *14*, 8379.

[27] T. Kanagawa, R. Hobara, I. Matsuda, T. Tanikawa, A. Natori, S. Hasegawa, *Phys. Rev. Lett.* **2003**, *91*, 036805.

[28] K. N. Altmann, J. N. Crain, A. Kirakosian, J. L. Lin, D. Y. Petrovykh, F. J. Himpsel, R. Losio, *Phys. Rev. B* **2001**, *64*, 035406.

[29] H. S. Yoon, S. J. Park, J. E. Lee, C. N. Whang, I. W. Lyo, *Phys. Rev. Lett.* **2004**, *92*, 096801.

[30] I. Barke, F. Zheng, A. R. Konicek, R. C. Hatch, F. J. Himpsel, *Phys. Rev. Lett.* **2006**, *96*, 216801.

[31] R. Schillinger, C. Bromberger, H. J. Jansch, H. Kleine, O. Kuhlert, C. Weindel, D. Fick, *Phys. Rev. B* **2005**, *72*, 115314.

[32] J. C. Charlier, X. Blase, S. Roche, *Rev. Mod. Phys.* **2007**, *79*, 677.

[33] D. Connetable, G. M. Rignanese, J. C. Charlier, X. Blase, *Phys. Rev. Lett.* **2005**, *94*, 015503.

[34] a) G. Lee, J. Guo, E. W. Plummer, *Phys. Rev. Lett.* **2005**, *95*, 116103; b) H. W. Yeom, S. Takeda, E. Rotenberg, I. Matsuda, K. Horikoshi, J. Schaefer, C. M. Lee, S. D. Kevan, T. Ohta, T. Nagao, S. Hasegawa, *Phys. Rev. Lett.* **1999**, *82*, 4898.

[35] P. C. Snijders, H. H. Weitering, *Rev. Mod. Phys.* **2010**, *82*, 307.

[36] a) C. Berger, Z. Song, X. Li, X. Wu, N. Brown, C. C. Naud, D. Mayou, T. Li, J. Hass, A. N. Marchenkov, E. H. Conrad, P. N. First, W. A. de Heer, *Science* **2006**, *312*, 1191; b) K. S. Novoselov, A. K. Geim, S. V. Morozov, D. Jiang, M. I. Katsnelson, I. V. Grigorieva, S. V. Dubonos, A. A. Firsov, *Nature* **2005**, *438*, 197.

[37] S. Yamazaki, Y. Hosomura, I. Matsuda, R. Hobara, T. Eguchi, Y. Hasegawa, S. Hasegawa, *Phys. Rev. Lett.* **2011**, *106*, 116802.

[38] J. N. Crain, A. Kirakosian, K. N. Altmann, C. Bromberger, S. C. Erwin, J. L. McChesney, J. L. Lin, F. J. Himpsel, *Phys. Rev. Lett.* **2003**, *90*, 176805.

[39] H. W. Yeom, Y. K. Kim, E. Y. Lee, K. D. Ryang, P. G. Kang, *Phys. Rev. Lett.* **2005**, *95*, 205504.

[40] C. Zeng, P. R. C. Kent, T.-H. Kim, A.-P. Li, H. H. Weitering, *Nat. Mater.* **2008**, *7*, 539.

[41] a) C. Tegenkamp, Z. Kallassy, H. Pfnur, H. L. Gunter, V. Zielasek, M. Henzler, *Phys. Rev. Lett.* **2005**, *95*, 176804; b) C. Tegenkamp, D. Lukermann, S. Akbari, M. Czubanowski, A. Schuster, H. Pfnur, *Phys. Rev. B* **2010**, *82*, 205413.

[42] S. Qin, T.-H. Kim, Y. Zhang, W. Ouyang, H. H. Weitering, C.-K. Shih, A. P. Baddorf, R. Wu, A.-P. Li, *Nano Lett.* **2012**, *12*, 938.

[43] S. Qin, S. Hellstrom, Z. Bao, B. Boyanov, A.-P. Li, *Appl. Phys. Lett.* **2012**, *100*, 103103.

[44] H. J. Mamin, P. H. Guethner, D. Rugar, *Phys. Rev. Lett.* **1990**, *65*, 2418.

[45] T.-H. Kim, X. G. Zhang, D. M. Nicholson, B. M. Evans, N. S. Kulkarni, B. Radhakrishnan, E. A. Kenik, A.-P. Li, *Nano Lett.* **2010**, *10*, 3096.

[46] Y. Kitaoka, T. Tono, S. Yoshimoto, T. Hirahara, S. Hasegawa, T. Ohba, *Appl. Phys. Lett.* **2009**, *95*, 052110.

[47] D. G. Brandon, *Acta Metall.* **1966**, *14*, 1479.

[48] T. Nemoto, T. Fukino, S. Tsurekawa, X. Gu, A. Teramoto, T. Ohmi, *Jpn. J. Appl. Phys.* **2009**, *48*, 066507.

[49] C. Schuster, M. Vangel, H. Schafft, *Microelectron. Reliab.* **2001**, *41*, 239.

[50] M. K. Srivastava, Y. Wang, X. G. Zhang, D. M. C. Nicholson, H.-P. Cheng, *Phys. Rev. B* **2012**, *86*, 075134.

[51] X. G. Zhang, W. H. Butler, *Phys. Rev. B* **1995**, *51*, 10085.

[52] T.-H. Kim, D. M. Nicholson, X.-G. Zhang, B. M. Evans, N. S. Kulkarni, E. A. Kenik, H. M. Meyer, B. Radhakrishnan, A.-P. Li, *Jpn. J. Appl. Phys.* **2011**, 50.

[53] K. Critchley, B. P. Khanal, M. Ł. Górzny, L. Vigderman, S. D. Evans, E. R. Zubarev, N. A. Kotov, *Adv. Mater.* **2010**, *22*, 2338.

[54] M. L. Gorzny, A. S. Walton, M. Wnek, P. G. Stockley, S. D. Evans, *Nanotechnology* **2008**, *19*, 165704.

[55] W. Fu, S. Qin, L. Liu, T.-H. Kim, S. Hellstrom, W. Wang, W. Liang, X. Bai, A.-P. Li, E. Wang, *Nano Lett.* **2011**, *11*, 1913.

[56] X. Lin, X. B. He, T. Z. Yang, W. Guo, D. X. Shi, H. J. Gao, D. D. D. Ma, S. T. Lee, F. Liu, X. C. Xie, *Appl. Phys. Lett.* **2006**, *89*, 043103.

[57] J. Homoth, M. Wenderoth, T. Druga, L. Winking, R. G. Ulbrich, C. A. Bobisch, B. Weyers, A. Bannani, E. Zubkov, A. M. Bernhart, M. R. Kaspers, R. Moller, *Nano Lett.* **2009**, *9*, 1588.
[58] S.-H. Ji, J. B. Hannon, R. M. Tromp, V. Perebeinos, J. Tersoff, F. M. Ross, *Nat. Mater.* **2011**, *11*, 114.
[59] K. C. Clark, et al., unpublished. **2013**.
[60] C. Joachim, *Atomic Scale Interconnection Machines*, Springer, Heidelberg **2012**.
[61] T.-H. Kim, M. Angst, B. Hu, R. Jin, X. G. Zhang, J. F. Wendelken, E. W. Plummer, A.-P. Li, *Proc. Natl. Acad. Sci. USA* **2010**, *107*, 5272.
[62] M. Aono, C.-S. Jiang, T. Nakayama, T. Okuda, S. Qiao, M. Sakurai, C. Thirstrup, Z.-H. Wu, *Oyo Buturi (Applied Physics–Monthly Journal of the Japan Society of Applied Physics)* **1998**, *67*, 1361 (Japanese).
[63] Y. Shingaya, T. Nakayamaa, M. Aono, *Physica B* **2002**, 323.
[64] T. Ikuno, M. Katayama, M. Kishida, K. Kamada, Y. Murata, T. Yasuda, S. Honda, J.-G. Lee, H. Mori, K. Oura, *Jpn. J. Appl. Phys.* **2004**, 43.
[65] T. H. Kim, R. Jin, L. R. Walker, J. Y. Howe, M. H. Pan, J. F. Wendelken, J. R. Thompson, A. S. Sefat, M. A. McGuire, B. C. Sales, D. Mandrus, A. P. Li, *Phys. Rev. B* **2009**, *80*, 214518.
[66] J. K. Gimzewski, B. Reihl, J. H. Coombs, R. R. Schlittler, *Z. Phys. B: Condens. Matter* **1988**, 72.